Journal of Materials Chemistry A

ROYAL SOCIETY OF CHEMISTRY

PAPER

View Article Online
View Journal | View Issue

Cite this: J. Mater. Chem. A, 2026, 14, 11651

Cross-talk and internal resistance in high-voltage graphite||$LiNi_{0.5}Mn_{1.5}O_4$ cells: sulfolane *vs.* carbonate-based electrolytes

Clément Pechberty, *[a] Eric Pui Lam Tam, [b] Julia Maibach [a] and Patrik Johansson [ac]

Received 10th November 2025
Accepted 10th February 2026

DOI: 10.1039/d5ta09119e

rsc.li/materials-a

High-voltage cathode active materials such as $LiNi_{0.5}Mn_{1.5}O_4$ offer promises of high-energy density lithium-ion batteries (LIBs), but their implementation is hindered by electrolyte instability and cross-talk phenomena that compromise cycling performance. This study presents a comprehensive investigation of interfacial degradation mechanisms in graphite||LNMO full cells, comparing a conventional carbonate-based electrolyte (1.0 M $LiPF_6$ in EC/DEC + 1 wt% LiBOB) with a sulfolane (SL)-based alternative (0.7 M LiBOB in SL + 0.2 M LiTFSI). Using the latter electrolyte results in reduced transition metal dissolution, but significant graphite coulombic efficiency degradation persists, as shown by a holistic assessment using graphite-limited cell configurations, *post mortem* analysis, and intermittent current interruption measurements. The cells with the SL-based electrolyte exhibit lower initial discharge capacities, reduced average coulombic efficiencies, and substantially higher LNMO interfacial resistances. They also produce organic rich interphases and soluble oxidation products affecting the anode performance, which rather than transition metal dissolution alone, constitute the dominant degradation pathway. Overall, the revealed complex interplay between electrolyte formulation, interfacial chemistry, and cross-talk mechanisms offers valuable insights for rational design of a next generation of electrolytes capable of supporting stable high-voltage LIB operation.

Introduction

High-voltage cathode active materials (CAMs) capable of enabling high-energy density lithium-ion batteries (LIBs) have attracted considerable interest in recent years.[1–5] $LiNi_{0.5}Mn_{1.5}O_4$ (LNMO), with an operating voltage of *ca.* 4.7 V *vs.* Li^+/Li and a theoretical capacity of 147 mA h g^{-1}, stands out as an exceptional candidate, capable of delivering LIB cells with an energy density of *ca.* 350 Wh L^{-1}.[6] The cobalt-free composition of LNMO also addresses the many concerns related to cost and unethical mining practices. In addition, LNMO exhibits excellent rate capability due to its three-dimensional Li^+ diffusion pathways and fast solid-state kinetics, enabling high-power operation without significant polarisation. This makes LNMO a very suitable and cost-effective CAM choice for high-power and high-energy density applications, such as electric vehicles.[4] Despite these principal benefits, LNMO faces significant challenges in practice; the high operating voltage induces severe anodic instability using conventional carbonate-based electrolytes. Furthermore, the interactions between LNMO and graphite—commonly referred to as cross-talk—result in additional degradation mechanisms, such as transition metal dissolution, leading to rapid capacity fading.[7]

In this context, alternative electrolytes based on more oxidation-resistant solvents are of interest, such as sulfones with their high dielectric permittivity and low flammability, but these face three key challenges: high melting points, high viscosities, and poor compatibility with graphite.[8] To address the latter, the use of alternative salts to lithium hexafluorophosphate ($LiPF_6$), as well as dual salt formulations, has been proposed.[9,10] Zhang *et al.*[10] studied the effect of various lithium salts on the electrochemical performance of ethylene sulfone-based electrolytes. Notably, those based on lithium difluoro(oxalato)borate (LiDFOB) exhibited the highest cycling stability, outperforming the commercial 1.0 M $LiPF_6$ in ethylene carbonate (EC)/diethyl carbonate (DEC) (3 : 7 w/w) electrolyte. Additionally, Salian *et al.*[11] demonstrated excellent performance of lithium bis(fluorosulfonyl)imide (LiFSI) in sulfolane (SL) in graphite||LNMO full cells. However, they also found that their SL-based electrolyte suffered from a higher degree of decomposition at high voltages as compared to carbonate-based electrolytes.[12]

[a]Department of Physics, Chalmers University of Technology, 412 96 Göteborg, Sweden. E-mail: clementp@chalmers.se
[b]Department of Industrial and Materials Science, Chalmers University of Technology, 412 96, Göteborg, Sweden
[c]ALISTORE-European Research Institute, FR CNRS 3104, Hub de L'Energie, Amiens 800 39, France

While recent studies have focused on improving the electrochemical stability of SL-based electrolytes in graphite||LNMO cells, a comprehensive understanding of the associated degradation mechanisms is still lacking. In particular, the compatibility of SL-based electrolytes with LNMO cathodes, their long-term interfacial evolution, including solid electrolyte interphase (SEI) and cathode electrolyte interphase (CEI) formation, and the impact of oxidative decomposition byproducts generated at high voltages on anode passivation and coulombic efficiency (C.E.) remain underexplored. Tracking *e.g.* the internal resistance (IR) can provide insight into the mechanisms underlying capacity fading.[5,11]

This study aims to clarify the origins and roles of interfacial degradation and cross-talk comparing two electrolytes; a conventional carbonate-based electrolyte: 1.0 M $LiPF_6$ in EC/DEC (1 : 1) + 1% lithium bis(oxalato)borate (LiBOB) (as an additive to reduce the transition metal dissolution),[10–13] and a SL-based electrolyte: 0.7 M LiBOB in SL + 0.2 M lithium bis(trifluoromethanesulfonyl)imide (LiTFSI). The SL-based electrolyte was specifically formulated to avoid the use of $LiPF_6$, thereby eliminating pathways for HF generation, while leveraging a dual-salt + sulfone strategy to enhance high-voltage stability.

Results and discussion

First, to assess the effect of LNMO-driven cross-talk on the C.E. of the graphite, full cells were assembled to be either LNMO-limited or graphite-limited w.r.t. capacity.[5,13] Second, *post mortem* characterisation of aged electrodes was carried out using several experimental techniques in order to gain a comprehensive understanding of the electrode interphases/interfaces created. Finally, we track the IR evolution using the intermittent current interruption (ICI) technique, which also enables us to indirectly and electrochemically monitor the evolution of the interphases/interfaces.

Cross-talk and C.E. by electrochemistry and analytic techniques

By using galvanostatic cycling of graphite||LNMO-limited full cells we can assess the difference in capacity retention and the LNMO C.E. between the SL- and carbonate-based electrolytes (Fig. 1a–c), which provides insight into the oxidative stability difference. Despite similar long-term stabilities, the two electrolytes exhibit distinctly different behaviours; after two formation cycles, the cell with the carbonate-based electrolyte delivers a higher discharge capacity ($\sim$120 mA h g^{-1}) than the SL-based one ($\sim$100 mA h g^{-1}), reflecting lower initial interfacial losses. This is consistent with the differences in C.E.: 85.3% and 97.1% *vs.* 76.8% and 96.8%, indicative of more parasitic reactions and a slower interphase stabilisation, in agreement with the literature.[11] Hence we obtain a more reactive interface using the SL-based electrolyte, likely driven by earlier on-set of oxidative decomposition of SL, LiBOB and LiTFSI.

At a C/3 rate, the cells with the SL-based electrolyte show greater polarisation, with larger charge/discharge overpotentials, indicative of larger interfacial resistances and slower charge-transfer kinetics. The high viscosity of SL[14,15] reduces the ionic conductivity and Li^+ mobility, while the inherently lower ionic conductivity of LiBOB-based electrolytes as compared to $LiPF_6$-based ones further amplifies these transport limitations.[16–18] As a result, concentration gradients and overpotentials are exacerbated, particularly at high voltages.[19] Consistently, after 150 cycles, the cells with the SL-based electrolyte deliver a lower average C.E. than the cells with the carbonate-based electrolyte, reflecting more irreversible lithium consumption (Table 1). Interestingly, the former show gradual C.E. recovery after $\sim$60 cycles, coinciding with capacity fading, suggesting that as reactive components decompose and accumulate at the interfaces, a progressively thicker, more stable interphase forms, enhancing the C.E. at the expense of capacity retention. However, this increase in C.E. may be attributed to the shorter cycle durations caused by the reduced capacity: less time spent at high voltages inherently limits exposure to oxidative conditions, thereby reducing the decomposition per cycle. Long-term cycling (Fig. S1) confirms faster capacity decay using the SL-based electrolyte. Chronoamperometry was performed at 4.9 V *vs.* Li^+/Li to directly assess the oxidation stability of both electrolytes *vs.* carbon-coated aluminium. Despite its lower C.E., the SL-based electrolyte exhibits lower oxidation currents than the carbonate-based electrolyte after 50 h (additional oxidation test, Fig. S15 and S16). This behaviour may result from the absence of porous carbon and transition metals, which can act as catalytic sites for electrolyte oxidation.

In order to quantify the metal cross talk contamination from the LNMO to the graphite electrode, ICP-MS was conducted on graphite anodes recovered after 150 discharges *vs.* LNMO (Fig. 1d and e). Despite the presence of 1 wt% of LiBOB in the carbonate-based electrolyte, the SL-based electrolyte results in less Mn accumulation (in agreement with the X-ray photoelectron spectroscopy (XPS) elemental analysis and energy dispersion X-ray spectroscopy (EDX) analysis: Fig. S2 and S3) as well as a lower Al concentration. The absence of any PF_6^--based hydrolysis and HF generation, which would lead to acidification of the electrolyte, might explain the reduced leaching. However, the non-negligible concentration of Mn could imply another source of acidification, potentially from oxalic and/or boric acid produced by LiBOB decomposition.[20] The higher lithium content in the SL-based electrolyte indicates a larger consumption due to either SEI-formation or more lithium being kinetically trapped in the graphite. Both electrolytes show very low levels of Ni and Cu contents below the detection limit, the latter implying negligible anode current collector corrosion.

To further elucidate the structural degradation of LNMO upon cycling, X-ray diffraction (XRD) was performed on pristine electrodes and those recovered after 150 cycles *versus* graphite with both electrolytes (Fig. 1f and g; profile matching in Fig. S4). All samples retained the disordered spinel structure ($Fd\bar{3}m$) without detectable secondary phases. However, the cycled electrodes exhibit a clear shift of the diffraction peaks toward higher angles and noticeable peak broadening. The refined lattice parameters (Table S1) reveal a contraction of approximately 0.80% $\pm$ 0.01% and 1.21% $\pm$ 0.01% for the carbonate-

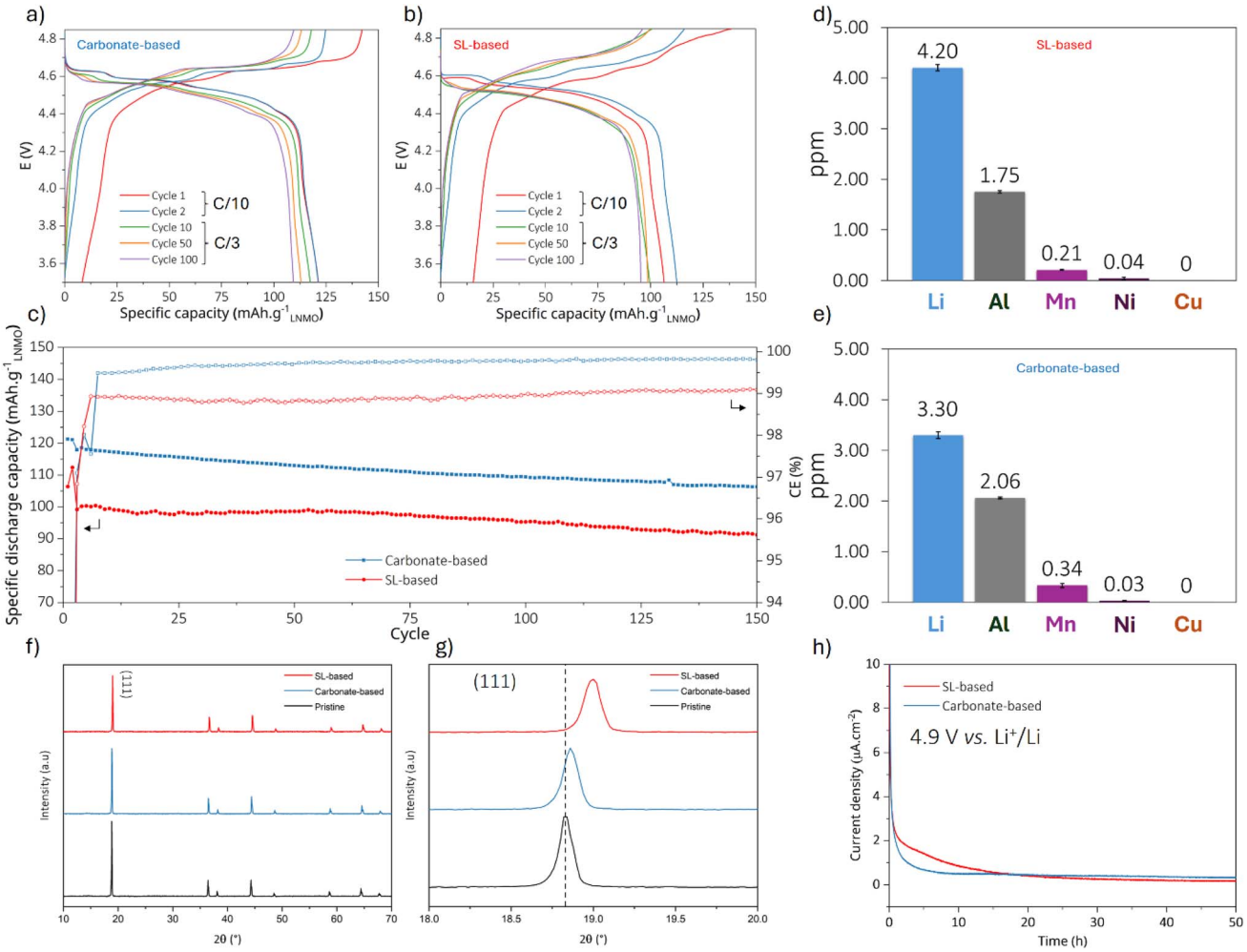

Fig. 1 Galvanostatic charge–discharge profiles of Graphite||LNMO cells using (a) the carbonate-based electrolyte and (b) the SL-based electrolyte. (c) Cycling stability and C.E. Concentrations of Li, Al, Mn, Ni, and Cu in the graphite electrode after 150 cycles *vs.* LNMO using (d) the SL-based and (e) the carbonate-based electrolytes (error bars represent the standard deviation from three samples). (f) XRD patterns of pristine LNMO and after 150 cycles *vs.* graphite using the carbonate- and SL-based electrolytes. (g) Magnified view of the (111) reflection. (h) Chronoamperometry at 4.9 V *vs.* Li^+/Li of the carbonate- and SL-based electrolyte using carbon coated Al working electrode.

Table 1 Average C.E. at constant C-rate for LNMO-limited cells (graphite as counter electrode) and graphite-limited cells (either LFP or LNMO as counter electrode), using carbonate-based and SL-based electrolytes

Cell	C.E. (%) carbonate-based electrolyte	C.E. (%) SL-based electrolyte
LNMO-limited *vs.* graphite	99.5	98.9
Graphite-limited *vs.* LFP	99.6	99.5
Graphite-limited *vs.* LNMO	99.2	98.8

and SL-based electrolytes, respectively, compared to the pristine LNMO. This lattice shrinkage is attributed to partial delithiation caused by the loss of cyclable lithium through parasitic reactions, consistent with the lower coulombic efficiency and faster capacity fading observed for the SL-based electrolyte.[3,21] The larger peak broadening observed using the SL-based electrolyte after cycling is consistent with the accumulation of microstrain and particle cracking within the LNMO structure, reflecting increased structural damage despite the reduced Mn dissolution.[22]

To investigate the effect of cross-talk on the graphite C.E., graphite-limited full cells were assembled in three-electrode configurations, using either LFP or LNMO as counter electrodes (Fig. 2), enabling direct monitoring of the graphite potential within the 0.01–1.00 V *vs.* Li^+/Li window, which is critical as it minimizes the risk of SEI breakdown induced by the high operating voltage of LNMO, as highlighted by Michalak *et al.*[23] Furthermore, maintaining the graphite potential above 0 V *vs.* Li^+/Li effectively eliminates the risk of Li plating. Under these conditions, the differences in C.E. can be attributed primarily to cathode-to-anode cross-talk. When LFP was used as the counter electrode, the graphite average C.E. remained

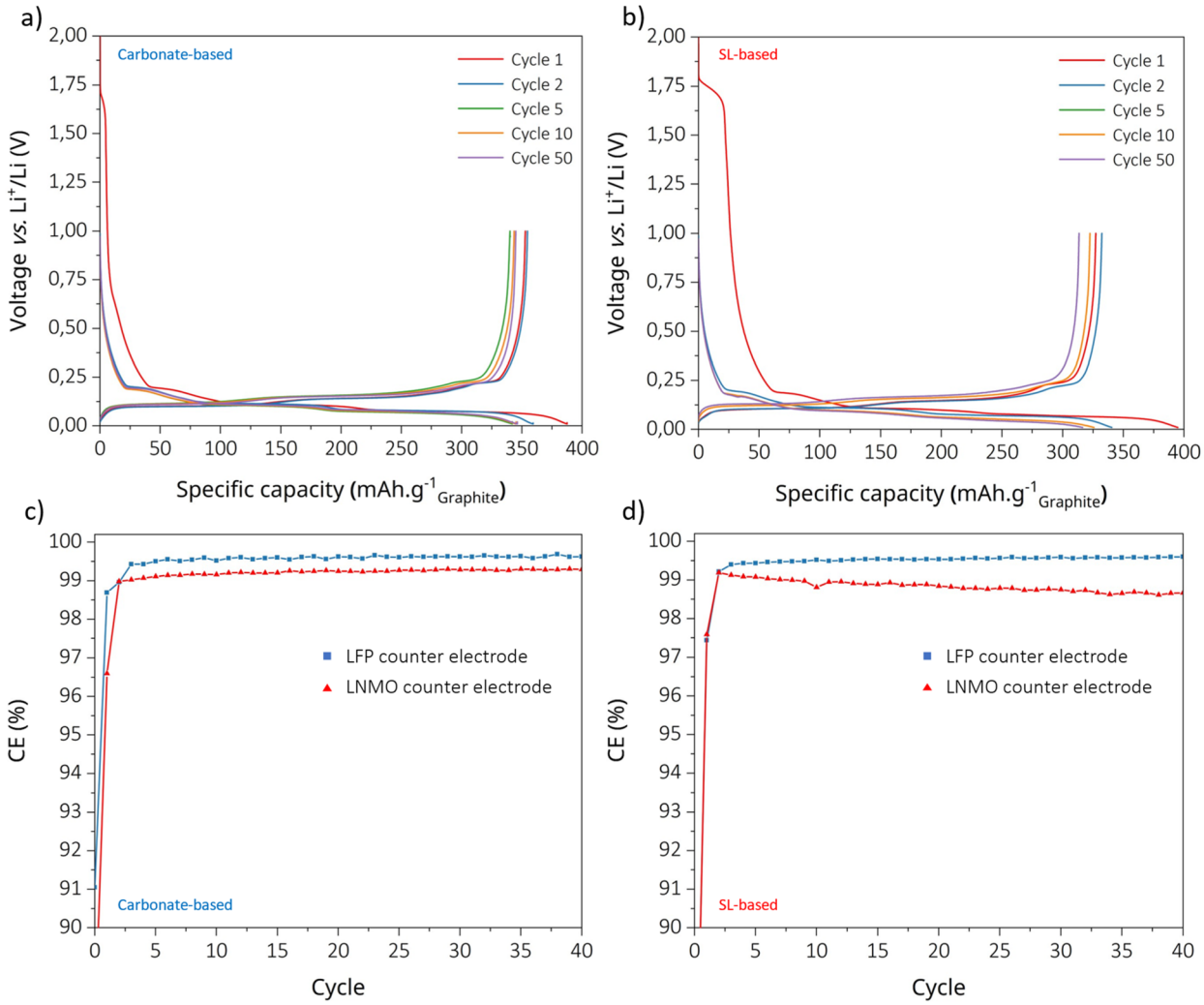

Fig. 2 Galvanostatic profile for the graphite side of three electrode graphite-limited||LNMO cells for: (a) the carbonate-based electrolyte, and (b) the SL-based electrolyte. C.E. of graphite using LFP (blue) or LNMO (red) as a counter electrode for: (c) the carbonate-based electrolyte, and (d) the SL-based electrolyte.

similar for both electrolytes, but when LNMO was used both cells exhibited lower C.E. (Table 1). Despite lower transition metal contamination using the SL-based electrolyte, a more pronounced decline in graphite C.E. was observed, in accordance with the higher concentration of Li detected in the ICP-MS measurement (Fig. 1). This indicates that, in addition to transition metal dissolution, other degradation mechanisms associated with the high-voltage cathode influence the graphite C.E. Previous studies have demonstrated that SL-based electrolytes generate less gas in graphite||LNMO cells as compared to when using a $LiPF_6$/carbonate-based electrolyte.[11,24,25] LiBOB decomposition has been linked to gas evolution (CO_2) on the LNMO side,[5,24,26,27] which also could possibly contribute to clogging of electrode and separator pores.[28] Furthermore, gaseous or dissolved CO_2 can diffuse to the graphite and undergo reduction to form lithium oxalate and/or lithium carbonate, thereby consuming lithium.[23,27] Other oxidation byproducts might dissolve in the electrolyte and react at the graphite anode, forming parasitic SEI components that also consume lithium. Altogether, these observations support the hypothesis that, although the SL-based electrolyte reduces transition metal leaching and minimises current collector corrosion, it promotes irreversible lithium losses through cross-talk mediated by soluble or gaseous degradation byproducts.

Surface analysis of LNMO electrodes

To investigate the composition of the CEI formed using the two electrolytes, XPS was performed on LNMO electrodes cycled for 100 discharges *vs.* graphite, as shown in Fig. 3, and compared with a pristine LNMO electrode. The C 1s spectra of the pristine electrode shows clear signals from sp^2 carbon (conductive carbon) and the CH_2/CF_2 groups from the polyvinylidene fluoride (PVDF) binder, along with minor contributions attributed to adsorbed species. The C 1s spectra for the cell cycled with the carbonate-based electrolyte shows signals from conductive carbon, hydrocarbon (C–H), alkoxy carbons (C–O), and carbonates (CO_3^{2-}), characteristic of a mixed organic/inorganic

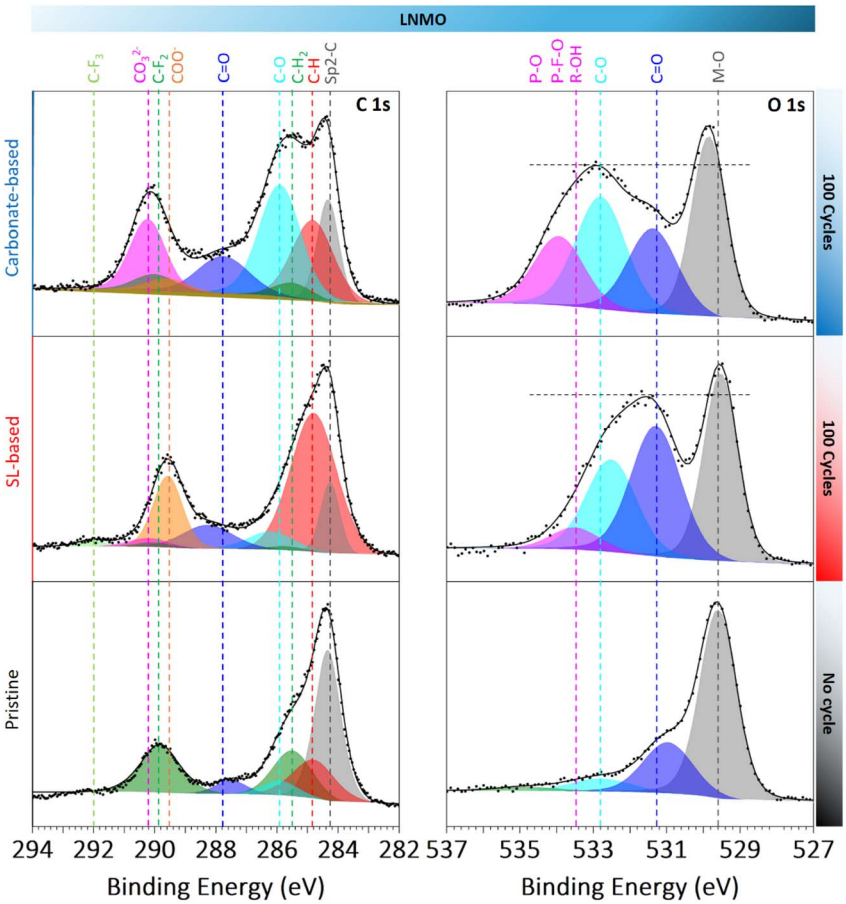

Fig. 3 XPS analysis of the C 1s and O 1s spectra for pristine LNMO and LNMO electrodes collected after 100 discharges using the carbonate-based and SL-based electrolytes.

CEI, formed by carbonate solvent and $LiPF_6$ decomposition into organic carbons and Li_2CO_3.[29] Additional smaller contributions could include carboxylates (COO^-, from EC ring-opening and LiBOB decomposition) and carbonyl species (C=O) from solvent breakdown.

In contrast, the LNMO electrode cycled using the SL-based electrolyte shows XPS spectra with more COO^- and C–H components and less CO_3^{2-}, C–O and C=O contributions. This indicates a CEI dominated by carboxylates species (R-COO^-) from SL and LiBOB oxidation. The S 2p spectra show only trace amounts of sulfuric species (from TFSI and SL decomposition), but the B 1s spectra show no boron-containing species for either electrolyte, suggesting boron-based LiBOB degradation products to be soluble rather than accumulating on the LNMO surface (Fig. S5).[5,26] The O 1s spectra further confirm this trend. Both samples display a sharp Metal–O signal from LNMO, along with additional C=O, C–O, and R–OH species, consistent with a complex mixture of organic products. While the CEI formed in the carbonate-based electrolyte shows a dominant C–O contribution with additional signal from P–F–O/P–O and R–OH, the CEI from the SL-based electrolyte exhibits a more pronounced C=O signal and a low R–OH contribution. Moreover, the relative intensity of the M–O peak to surface-related species is lower using the SL-based electrolyte, implying a slightly thicker CEI within the XPS probing depth (~8–9 nm).[30]

Overall, the CEI formed using the SL-based electrolyte is dominated by carboxylate species resulting mostly from the concurrent oxidation of the SL solvent and the LiBOB salt. While the specific contribution of the solvent *versus* the salt to these degradation products is difficult to decouple, the spectra are consistent with the accumulation of oxidation products potentially as R-COO^- species. The relatively low C.E. of LNMO with the SL-based electrolyte (Fig. 1), combined with the presence of a thin CEI, suggests the possible generation of gaseous byproducts such as CO_2,[5,24,27,28] as well as soluble R-COO^- and boron-containing fragments. These species, together with CO_2, may diffuse toward the graphite electrode, promote cross-talk reactions, and ultimately lower the C.E of graphite.

Surface analysis of graphite electrodes

To probe the SEI composition, XPS was also performed on graphite electrodes, recovered after 1 and 100 discharges *vs.* LNMO and compared to a pristine LNMO electrode to directly evidence cross talk species (Fig. 4). The C 1s spectrum of the pristine electrode shows an intense sp^2 carbon signal attributed to graphitic carbon accompanied by a C–H peak. Additional

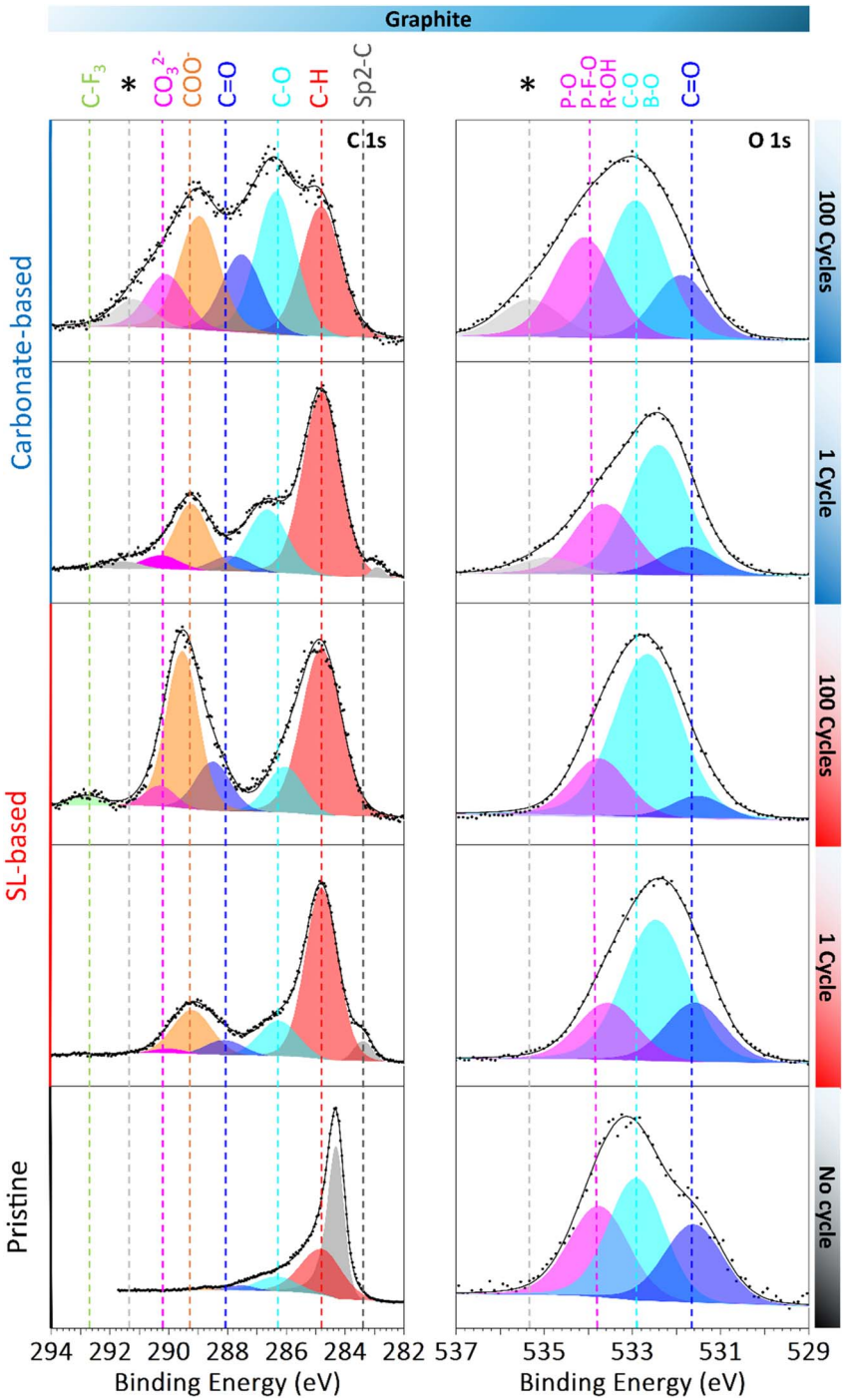

Fig. 4 XPS analysis of C 1s and O 1s for pristine graphite and graphite electrodes collected after 1 and 100 discharges with the carbonate-based electrolyte and the SL-based electrolyte.

weak signals can be attributed to oxidised carbon likely due to the carboxymethyl cellulose (CMC) binder and adsorbed species. After 1 cycle with the carbonate-based electrolyte XPS analysis renders a C 1s spectrum with dominant contributions from C–H, along with C–O, and COO^- signals consistent with an SEI rich in alkoxy and carboxylate species. Additional weaker feature corresponding to CO_3^{2-}, C=O and sp^2-C from graphite were also detected.[30] From 1 to 100 cycles, all contributions except the C–H increase in intensity, while the graphite peak has disappeared, indicating a thickening of the SEI.

In contrast, after 1 cycle with the SL-based electrolyte, the C 1s spectrum displays dominant C–H and COO^- peaks with minor contributions from C=O, C–O and CO_3^{2-} species. Part of the COO^- signal can be attributed to lithium oxalate formation,[20,31] likely originating from LiBOB reduction during the initial cycle, as indicated by the plateau at 1.8 V *vs.* Li^+/Li

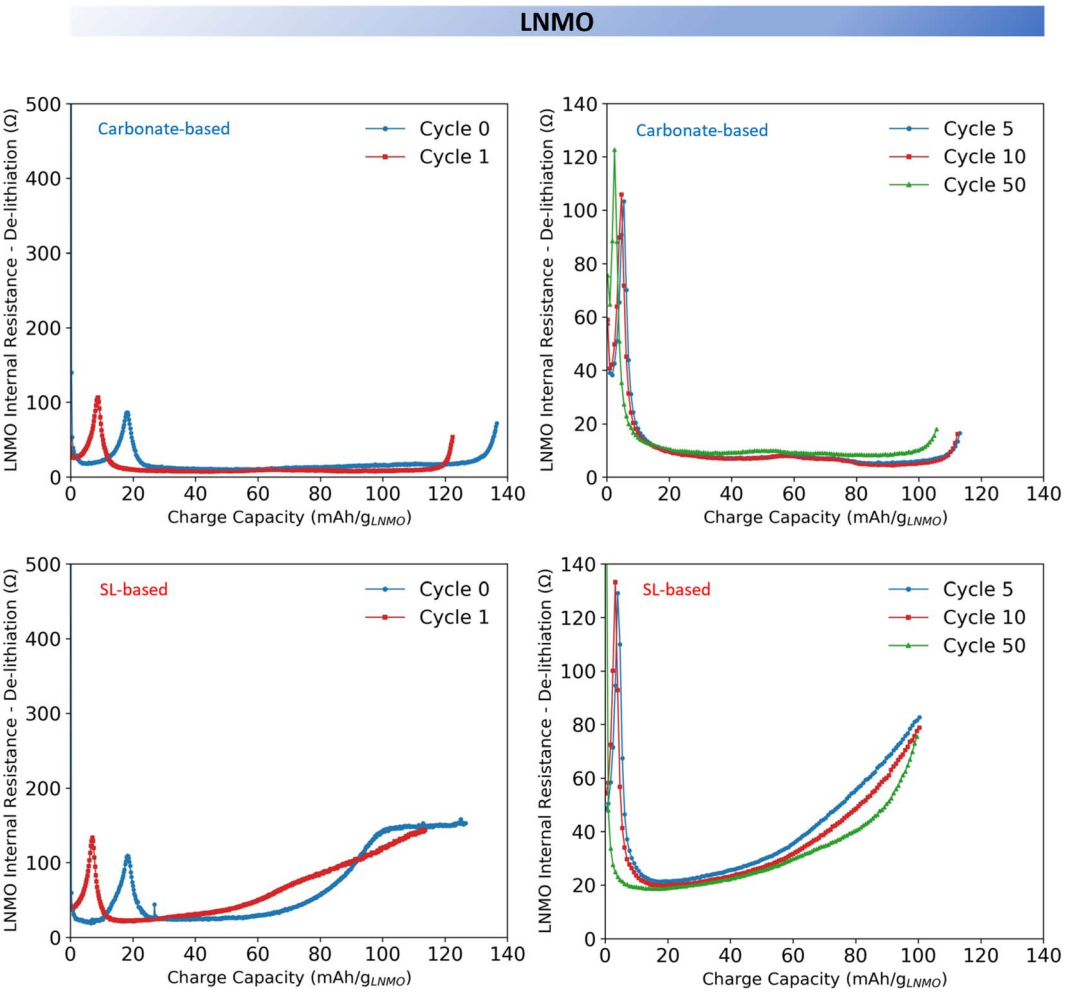

Fig. 5 Internal resistance tracking of 18 mm LNMO electrode during charging in three-electrode cells using either the carbonate-based or the SL-based electrolyte.

(Fig. 2).[31] From the 1st to the 100th cycle, a C–F_3 component appears, indicating TFSI decomposition, accompanied by an overall increase in all oxidised carbon peaks. Markedly, the COO^- signal greatly increases. This likely reflects the contribution from the reduction of species produced at the cathode side, such as CO_2 or R-COO^- fragments. Additionally, the sp^2-carbon peak from the underlying graphite, still visible after 1 cycle, becomes fully attenuated by the overlying SEI. The O 1s spectra further differentiate the SEIs; using the SL-based electrolyte, the SEI exhibits a dominant C–O contribution, consistent with alkoxy, borate-ester and sulfonyl fragments. In contrast, using the carbonate-based electrolyte shows larger C=O and P–O/R–OH contributions. Minor features at 535.3 eV on the O 1s and 291.4 eV on the C 1s (indicated with a *) possibly due to important charging effects can be observed. An extra peak is also visible both on the C 1s and O 1s spectra. As opposed to LNMO and its visible M–O peak in the O 1s spectra, the SEI on graphite appears substantially thicker than the CEI on LNMO, exceeding the XPS probing depth (~8–9 nm) with both electrolytes. Boron was clearly identified in the B 1s spectrum with both electrolyte (Fig. S7) to a greater extent with the SL-based electrolyte, confirming incorporation of LiBOB-derived B-O_x decomposition products into the SEI through local reduction, possibly as cross-linked oligomeric borates.[20] However, LiF was only observed with the carbonate-based electrolyte from the first cycle (Fig. S7). Using the carbonate-based electrolyte, Mn signals were detected in the Mn 2p and Mn 3p spectra on the graphite electrodes (Fig. S7), suggesting transition metal dissolution from LNMO and deposition on graphite.[29] In contrast, the graphite electrodes cycled using the SL-based electrolyte showed no Mn signal. Only after sputtering did a weak Mn signal emerge (Fig. S2), in agreement with ICP-MS results and indicating reduced, yet measurable, Mn deposition buried beneath the surface of the SEI.

Overall, using the SL-based electrolyte appears to mitigate Mn cross-talk. However, the marked decline in graphite C.E. (Fig. 2). suggests a cross-talk mechanism possibly driven by the diffusion and reduction of CO_2 and other soluble oxidative byproducts, such as R-COO^- fragments, forming most likely lithium oxalate on the graphite surface.

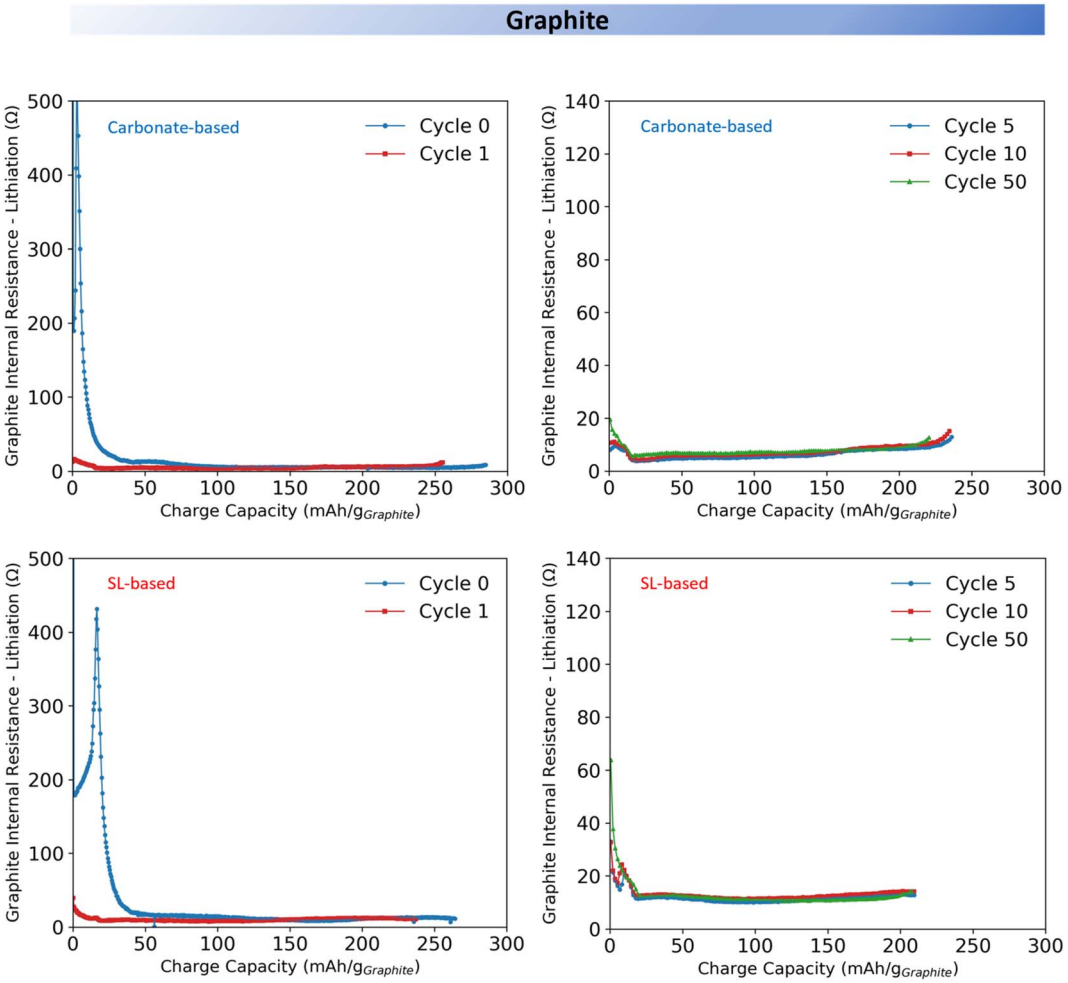

Fig. 6 Internal resistance tracking of 18 mm graphite electrode during charging in three-electrode cells using either the carbonate-based or the SL-based electrolyte.

Internal resistance tracking for LNMO electrodes

To better understand the influence of electrolyte composition on interfacial properties and especially the evolution of the IR, graphite||LNMO three electrode cells were cycled using the ICI protocol (Fig. 5 and 6) (see Experimental section and Fig. S10 and S11).

Measurements were performed using a three-electrode cell configuration to isolate the contribution of the anode and the cathode. The IR was calculated from the voltage drop 1 second after current interruption. This value represents a summation of the ohmic resistance (ionic resistance of the bulk electrolyte as well as the electronic resistance of the electrodes and the current collectors), the charge transfer resistance (R_{ct}) associated with interfacial kinetics (including overpotential caused by the redox reaction), the electrodes film resistance (R_{film}) and a limited contribution from diffusion resistance due to the 1 second timescale. While the absolute value of the ohmic resistance typically remain stable in early cycles, the significant variations observed in the IR are primarily driven by the evolution of the interfacial resistances (R_{ct} and R_{film}). However, as it is difficult to precisely segregate which specific interface phenomenon is responsible for the increase in IR, this measurement serves as an indicator of the global interface stability.[11,32,33] For the carbonate-based electrolyte, the IR of the LNMO cathode remained relatively stable across the full state of charge (SOC) range during both charging (Fig. 5) and discharging (Fig. S13). In contrast, the SL-based electrolyte induced markedly different IR behaviour (Fig. 5); during the first formation cycle it rose sharply at ~60% SOC (80 mA h g^{-1}; >4.7 V *vs.* Li$^+$/Li), followed by a short plateau, and in subsequent cycles, the increase became more gradual and consistently relaxed during the discharge (Fig. S13). The former could correspond to the onset of CEI formation *via* oxidative decomposition of LiBOB, SL, and residual impurities. The IR build-up, on the other hand, might suggests an incomplete and poorly passivating CEI growth, likely due to the dominance of organic species. The large solubility of oxidation products at the LNMO interface may further hinder stable CEI formation, as well as possible gas evolution (*e.g.*, CO_2) could clog the electrode and separator pores resulting in increased IR by blocking active surface sites.[27,28,34] As a result, the interphase remains highly voltage-sensitive, leading to increased overpotentials, reduced

rate capability, and accelerated capacity fade, all relative to the carbonate-based electrolyte.

After 50 cycles, the carbonate-based electrolyte showed a slight increase in LNMO IR. The three-electrode cycling profiles (Fig. S12) confirm that the maximum voltage on the cathode side remained constant, ruling out increased IR due to any rising cathode potential, thus the minor IR increase could be attributed to a gradual interphase growth and/or increased bulk electrolyte resistance. In contrast, the cells using the SL-based electrolyte exhibited a markedly different behaviour; a slight decrease in IR while the three-electrode cycling profile (Fig. S11) showed a stable maximum cathode voltage. This may reflect a slow reorganisation or densification of the CEI, potentially due to the continued dissolution of surface oxidation products and delayed accumulation of poorly passivating organic species. Yet, the median IR of LNMO using the SL-based electrolyte is approximately five times that of using the carbonate-based electrolyte (Fig. S14).

Internal resistance tracking for graphite electrodes

For both electrolytes, the graphite IR remained relatively stable across the full SOC range during the formation charge (Fig. 6) and discharge cycle (Fig. S13), besides from an initial sharp peak attributed to SEI formation by LiBOB decomposition.[11] After 50 cycles, the IR of graphite using the carbonate-based electrolyte slightly increases, likely due to gradual interphase growth or increased bulk electrolyte resistance. In contrast, using the SL-based electrolyte the IR remained essentially constant. However, the C.E. assessment (Fig. 2) indicated a poorer SEI in the cell with the SL-based electrolyte and thus the absence of any IR increase may therefore reflect masking effects from elevated polarisation or interfacial overpotentials that are not fully captured in the analysis.

Conclusion

Revealing the degradation mechanisms in high-voltage graphite||LNMO cells provides key insights into the origins of the contrasting behaviour resulting from using conventional carbonate- *vs.* alternative SL-based electrolytes. The electrolyte composition governs the interfacial stability; while the SL-based electrolyte reduces transition metal dissolution and current collector corrosion, it also introduces degradation pathways that compromise overall cell performance by creating abundant soluble or gaseous byproducts. The diffusion of these species to the graphite anode leads to further parasitic reactions. These findings challenge the prevailing view that cross-talk in high-voltage cells is dominated by transition metal dissolution and highlights the need for a more holistic electrolyte design strategy that simultaneously addresses oxidative stability, interfacial passivation, and electrolyte byproduct solubility.

Future electrolyte development efforts should thus prioritise formulations that minimise both transition metal dissolution and soluble oxidation product formation. Here additives that promote inorganic CEI formation, alongside a controlled viscosity modulation to balance transport properties with interfacial stability can be one path, together with salt combinations that synergistically enhance passivation while maintaining electrochemical stability.

Experimental methods

Electrode preparation

LNMO and graphite electrodes were provided by MORROW Batteries (Norway). They contained 97% and 96% of active material, respectively, for areal capacities of 1.41 and 1.76 mA h cm^{-2} (10.5 and 5.03 mg_{AM} cm^{-2} corresponding to a N/P ratio of about 1.25). The binder used for the LNMO electrodes was PVDF while, a mix of CMC and Styrene-Butadiene Rubber (SBR) was used for the graphite electrodes. Additional 2.42 mA h cm^{-2} LNMO (MORROW) and 3.5 mA h cm^{-2} LFP (Custom cell) electrodes were used for the graphite-limited cells. Reference electrodes were prepared using either a 0.125 mm Ø polyimide insulated Cu wire (Goodfellow, 99.99%) or a ring of Li metal (El cell, outer and inner Ø of 21.6 and 20.6 mm, respectively). For the wire, the insulation was removed on the first 2 mm, then a piece of Li was folded over the tip to form a needle shape reference of about 1 mm width at the base (Fig. S18). All air and moisture sensitive operation were carried out in a Vigor argon filled glovebox maintained below 0.5 ppm of O_2 and H_2O.

Electrolyte preparation

To prepare the electrolytes, SL (Fisher scientific, 99+%) was maintained liquid at 40 °C in an argon-filled glove box and dried with molecular sieves for a week. A water content <10 ppm was determined by Karl Fisher titration. EC and DEC (Sigma Aldrich, ≥99%, H_2O < 10 ppm) were used as received. $LiPF_6$ (Sigma Aldrich, 99.99%) was dried at 70 °C under vacuum for 24 h. LiBOB (Sigma Aldrich, ≥98.5%) and LiTFSI (Solvionic, 99.99%) were both dried at 120 °C for 24 h. The carbonate-based electrolyte was prepared by dissolving 1.0 M of $LiPF_6$ in EC and DEC 1 : 1 v/v. The SL-based electrolyte was prepared by dissolving 0.7 M of LiBOB and 0.2 M of LiTFSI in SL. Both electrolytes were stirred until clear solutions were obtained.

Cell assembly

Coin cells (2032, Hohsen, 316L, Al coated casing) were assembled in an argon-filled glove box using 10 mm diameter graphite, LNMO, or LFP electrodes and a single 16 mm glass fibre separator (GF/C) filled with 60 μL of electrolyte. For the three-electrode graphite-limited cells, a wired Li metal reference electrode was added between two 16 mm GF/C separators before sealing the cell (Fig. S17). The seal was improved by adding epoxy resin around the reference wire.[35] Pat cells (El cell) used for ICI were assembled in an argon-filled glove box using 18 mm diameter electrodes, ring-shaped Li metal reference electrode and a 21.8 mm diameter glass fibre separator (GF/A specific diameter provided by El cell). Aluminium and stainless-steel plungers were used for the LNMO and graphite side, respectively.

Electrochemical characterisation

Graphite-limited cells were cycled between 0.01 and 1.00 V *vs.* Li^+/Li with two formation cycles at C/13.5 followed by a C/4.1 rate. All two electrode full cells were cycled between 3.50 and 4.85 V with two formation cycles at C/10 followed by a C/3 rate (1C corresponding to 0.864 mA cm^{-2}). The ICI measurement was performed in a three-electrode Pat cell (Fig. S10) with current interruptions of 1 s every minute. The calculation of the IR was made by dividing the voltage drop after 1 s by ΔI according to Ohm's law ($R = \Delta E_{1s}/\Delta I$) as seen in previous studies.[11,36,37] Data analysis was performed using Python (code available Fig. S12). All electrochemical characterisations were performed at ambient temperature and repeated at least two times using a Biologic VMP3, Biologic MPG2, or Landt potentiostat.

Surface characterisation

Prior to XPS and scanning electron microscopy (SEM) coupled with EDX analyses, the electrode samples were washed in 1 ml of dimethyl carbonate (DMC) and dried inside an argon-filled glove box. The samples were transferred using an airtight transfer system to avoid any exposure to air. XPS measurements were performed using a PHI-5000 VersaProbe III instrument equipped with a monochromatic Al Kα X-ray source ($E = 1486.6$ eV). The binding energy scale was calibrated with reference to the characteristic peaks of the sputter-cleaned gold (Au), silver (Ag) and copper (Cu) foils, which corresponds to 83.96 eV (Au $4f_{7/2}$), 368.21 eV (Ag $3d_{5/2}$) and 932.62 eV (Cu $2p_{3/2}$), respectively, according to ISO 15472:2010 standard. Prior to analysis, the data was calibrated by aligning the carbon spectra (C 1s) at 284.8 eV in response to the adventitious carbon. XPS fitting was performed in CasaXPS software using a Shirley background function. Due to the complex nature and many different carbon components in the CEI and SEI, we developed a fitting model based on previously reported peak positions for the individual carbon components. To ensure a consistent and physically meaningful deconvolution, a constrained fitting model was developed based on established binding energies. Peak positions were restricted to characteristic chemical shifts relative to the C–H reference, with a maximum allowed deviation of ± 0.2 eV. Additionally, the separation between the C–H_2 and C–F_2 peaks of the PVDF binder was constrained to 4.5 eV. For the graphitic sp^2-C signal on the pristine electrode, LA(50) line shape with asymmetric parameters was applied; for all other components, the asymmetry parameters were set to their default values (effectively symmetric). To prevent overfitting, strict constraints were applied: the FWHM of the sp_2-C peak was constrained to 0.8 ± 0.1 eV, while all other carbon components were constrained to 1.6 ± 0.2 eV (except for the C=O peak of the LNMO electrode which was set to 2 eV). SEM and EDX analyses were conducted on a Tescan GAIA3 operated at an accelerating voltage of 10 kV and a working distance of 10 mm.

ICP-MS

The graphite electrodes were first washed with 1 ml of DMC and dried in the glove box. Then, the coating was removed from the Cu current collector and digested in 3 ml of 69% HNO_3 and stirred for 6 h at 90 °C. After cooling down, 1 ml of H_2O_2 was added and the solution was stirred overnight to oxidise graphite. Finally, the solution was diluted 10 times using ultrapure water.

XRD

The LNMO electrodes recovered after 150 cycles were washed with the same procedure as the for the previous characterisations. A piece of Kapton film was used on the XRD holder to limit contact with air and moisture. XRD measurements were performed on a Bruker D8 discover diffractometer operating with Cu Kα radiation. EVA software was used to refine the lattice parameter and determine the FWHM.

Author contributions

C. P. conceived the idea for this work, designed the study, formulated the electrolytes, performed the electrochemical characterisation, analysed and interpreted the data, and prepared the initial draft of the manuscript. E. T. performed the XPS measurements. J. M. assisted with the XPS interpretation. P. J. provided mentoring, secured funding, and managed the project. All authors revised and accepted the final version of this manuscript.

Conflicts of interest

The authors declare no competing financial interests.

Data availability

The data supporting this article have been included as part of the supplementary information (SI). Supplementary information is available. See DOI: https://doi.org/10.1039/d5ta09119e.

Acknowledgements

The authors gratefully acknowledge: the financial support from the Swedish Energy Agency (P2022-00024); MORROW Batteries and especially Dr Adriana Navarro-Suarez for providing the electrodes; Dr Ezio Zanghellini for his valuable technical assistance; Dr Amanda Persdotter for performing the SEM/EDX imaging; Dr Stellan Holgersson for running the ICP-MS measurements; Dr Zaher Slim and Dr Patricia Huijbers for help with manuscript review and editing, and finally C. P. acknowledges the use of ChatGPT from OpenAI for manuscript editing.

References

1 X. Zhu, A. Huang, I. Martens, N. Vostrov, Y. Sun, M. I. Richard, T. U. Schülli and L. Wang, High-Voltage Spinel Cathode Materials: Navigating the Structural Evolution for Lithium-Ion Batteries, *Adv. Mater.*, 2024, **36**(30), DOI: 10.1002/adma.202403482.

2 J. Liu, S. He, S. Liu, S. Wang and J. Zhang, Advanced electrolyte systems with additives for high-cell-voltage and high-energy-density lithium batteries, *J. Mater. Chem. A*, 2022, (43), 22929–22954, DOI: 10.1039/d2ta07696a.

3 W. Bao, W. Yao, Y. Li, B. Sayahpour, B. Han, G. Raghavendran, R. Shimizu, A. Cronk, M. Zhang, W. Li and Y. S. Meng, Insights into lithium inventory quantification of $LiNi_{0.5}Mn_{1.5}O_4$–graphite full cells, *Energy Environ. Sci.*, 2024, **17**(12), 4263–4272, DOI: 10.1039/D4EE00842A.

4 W. Li, Y. G. Cho, W. Yao, Y. Li, A. Cronk, R. Shimizu, M. A. Schroeder, Y. Fu, F. Zou, V. Battaglia, A. Manthiram, M. Zhang and Y. S. Meng, Enabling high areal capacity for Co-free high voltage spinel materials in next-generation Li-ion batteries, *J. Power Sources*, 2020, **473**, DOI: 10.1016/j.jpowsour.2020.228579.

5 B. Aktekin, M. J. Lacey, T. Nordh, R. Younesi, C. Tengstedt, W. Zipprich, D. Brandell and K. Edström, Understanding the Capacity Loss in $LiNi_{0.5}Mn_{1.5}O_4$–$Li_4Ti_5O_{12}$ Lithium-Ion Cells at Ambient and Elevated Temperatures, *J. Phys. Chem. C*, 2018, **122**(21), 11234–11248, DOI: 10.1021/acs.jpcc.8b02204.

6 C. Fink Elkjaer and J. Højberg, *Technical status for Topsoe*, Whitepaper, Topsoe, 2023.

7 C. R. Birkl, M. R. Roberts, E. McTurk, P. G. Bruce and D. A. Howey, Degradation diagnostics for lithium ion cells, *J. Power Sources*, 2017, **341**, 373–386, DOI: 10.1016/j.jpowsour.2016.12.011.

8 X. Fan and C. Wang, High-voltage liquid electrolytes for Li batteries: progress and perspectives, *Chem. Soc. Rev.*, 2021, **50**, 10486–10566, DOI: 10.1039/D1CS00450F.

9 L. Lv, H. Zhang, D. Lu, Y. Yu, J. Qi, J. Zhang, S. Zhang, R. Li, T. Deng, L. Chen and X. Fan, A low-concentration sulfone electrolyte enables high-voltage chemistry of lithium-ion batteries, *Energy Mater.*, 2022, **2**, 200030, DOI: 10.20517/energymater.2022.38.

10 T. Zhang, W. Porcher and E. Paillard, Towards practical sulfolane based electrolytes: Choice of Li salt for graphite electrode operation, *J. Power Sources*, 2018, **395**, 212–220, DOI: 10.1016/j.jpowsour.2018.05.077.

11 G. D. Salian, A. Mathew, R. Gond, W. van Ekeren, J. Højberg, C. Fink Elkjær, M. J. Lacey, S. K. Heiskanen, D. Brandell and R. Younesi, Understanding the Electrochemical and Interfacial Behavior of Sulfolane based Electrolyte in $LiNi_{0.5}Mn_{1.5}O_4$-Graphite Full-Cells, *Batteries & Supercaps*, 2023, **6**(5), DOI: 10.1002/batt.202200565.

12 K. Xu and C. A. Angell, Sulfone-Based Electrolytes for Lithium-Ion Batteries, *J. Electrochem. Soc.*, 2002, **149**, A920, DOI: 10.1149/1.148386.

13 S. R. Li, C. H. Chen, X. Xia and J. R. Dahn, The Impact of Electrolyte Oxidation Products in $LiNi_{0.5}Mn_{1.5}O_4$/$Li_4Ti_5O_{12}$ Cells, *J. Electrochem. Soc.*, 2013, **160**, A1524–A1528, DOI: 10.1149/2.051309jes.

14 P. H. Luu, P. H. Tran, H. Van Nguyen, A. L. B. Phan, O. H. Nguyen, M. Van Tran, P. M. L. Le and T. D. Vo, Sulfolane as a co-solvent for carbonate-electrolytes in lithium-ion batteries using a $LiMn_2O_4$ cathode, *Vietnam Journal of Science, Technology and Engineering*, 2022, **64**, DOI: 10.31276/VJSTE.64(1).09-13.

15 Y. Ugata, G. Hasegawa, N. Kuwata, K. Ueno, M. Watanabe and K. Dokko, Temperature Dependency of Ion Transport in Highly Concentrated Li Salt/Sulfolane Electrolyte Solutions, *J. Phys. Chem. C*, 2022, **126**(45), 19084–19090, DOI: 10.1021/acs.jpcc.2c06699.

16 J. Li, J. Yang, Z. Ji, M. Su, H. Li, Y. Wu, X. Su and Z. Zhang, Prospective Application, Mechanism, and Deficiency of Lithium Bis(oxalate)Borate as the Electrolyte Additive for Lithium-Batteries, *Adv. Energy Mater.*, 2023, **13**, 35, DOI: 10.1002/aenm.202301422.

17 F. Azeez and P. S. Fedkiw, Conductivity of libob-based electrolyte for lithium-ion batteries, *J. Power Sources*, 2010, **195**, 7627–7633, DOI: 10.1016/j.jpowsour.2010.06.021.

18 S. Li, Y. Zhao, X. Shi, B. Li, X. Xu, W. Zhao and X. Cui, Effect of sulfolane on the performance of lithium bis(oxalato) borate-based electrolytes for advanced lithium ion batteries, *Electrochim. Acta*, 2012, **65**, 221–227, DOI: 10.1016/j.electacta.2012.01.052.

19 S. Tan, Z. Shadike, X. Cai, R. Lin, A. Kludze, O. Borodin, B. L. Lucht, C. Wang, E. Hu, K. Xu and X. Q. Yang, Review on Low-Temperature Electrolytes for Lithium-Ion and Lithium Metal Batteries, *Electrochem. Energy Rev.*, 2023, **6**, 35, DOI: 10.1007/s41918-023-00199-1.

20 B. S. Parimalam and B. L. Lucht, Reduction Reactions of Electrolyte Salts for Lithium Ion Batteries: $LiPF_6$, $LiBF_4$, LiDFOB, LiBOB, and LiTFSI, *J. Electrochem. Soc.*, 2018, **165**(2), A251, DOI: 10.1149/2.0901802jes.

21 W. Yao, Y. Li, M. Olguin, S. Bai, M. A. Schroeder, W. Li, A. Liu, N. R. Park, B. Bhamwala, B. Sayahpour, G. Raghavendran, O. Borodin, M. Zhang and Y. S. Meng, Stabilizing high temperature operation and calendar life of $LiNi_{0.5}Mn_{1.5}O_4$, *Next Energy*, 2024, **4**, 100136, DOI: 10.1016/j.nxener.2024.100136.

22 T. Kozawa, Lattice deformation of $LiNi_{0.5}Mn_{1.5}O_4$ spinel cathode for Li-ion batteries by ball milling, *J. Power Sources*, 2019, **419**, 52–57, DOI: 10.1016/j.jpowsour.2019.02.063.

23 B. Michalak, B. B. Berkes, H. Sommer, T. Brezesinski and J. Janek, Electrochemical Cross-Talk Leading to Gas Evolution and Capacity Fade in $LiNi_{0.5}Mn_{1.5}O_4$/Graphite Full-Cells, *J. Phys. Chem. C*, 2016, **121**(1), 211–216, DOI: 10.1021/acs.jpcc.6b11184.

24 C. Misiewicz, K. Edstrom and E. J. Berg, Formation of a Cathode Electrolyte Interphase on High-Voltage Li-ion Cathodes, *Chem. Mater.*, 2024, **36**(19), 9729–9740, DOI: 10.1021/acs.chemmater.4c01872.

25 J. Xia, J. Self, L. Ma and J. R. Dahn, Sulfolane-Based Electrolyte for High Voltage $Li(Ni_{0.42}Mn_{0.42}Co_{0.16})O_2$ (NMC442)/Graphite Pouch Cells, *J. Electrochem. Soc.*, 2015, **162**(8), A1424–A1431, DOI: 10.1149/2.0121508jes.

26 M. Xu, N. Tsiouvaras, A. Garsuch, H. A. Gasteiger and B. L. Lucht, Generation of Cathode Passivation Films via Oxidation of Lithium Bis(oxalato) Borate on High Voltage Spinel ($LiNi_{0.5}Mn_{1.5}O_4$), *J. Phys. Chem. C*, 2014, **118**(14), 7363–7368, DOI: 10.1021/jp501970j.

27 B. Michalak, B. B. Berkes, H. Sommer, T. Bergfeldt, T. Brezesinski and J. Janek, Electrochemical Cross-Talk Leading to Gas Evolution and Capacity Fade in $LiNi_{0.5}Mn_{1.5}O_4$/Graphite Full-Cells, *Anal. Chem.*, 2016, **121**(1), 211–216, DOI: 10.1021/acs.jpcc.6b11184.

28 B. Michalak, H. Sommer, D. Mannes, A. Kaestner, T. Brezesinski and J. Janek, Gas Evolution in Operating Lithium-Ion Batteries Studied In Situ by Neutron Imaging, *Sci. Rep.*, 2015, **5**, 15627, DOI: 10.1038/srep15627.

29 R. Azmi, F. Lindgren, K. Stokes-Rodriguez, M. Buga, C. Ungureanu, T. Gouveia, I. Christensen, S. Pal, A. Vlad, A. Ladam, K. Edström and M. Hahlin, An XPS Study of Electrolytes for Li-Ion Batteries in Full Cell LNMO vs Si/Graphite, *ACS Appl. Mater. Interfaces*, 2024, **16**(26), 34266–34280, DOI: 10.1021/acsami.4c01891.

30 XPS analysis of solid-electrolyte interphase layer formed on a lithium-ion battery negative electrode, *Kratos Analytical, MO496(A)*, 2022.

31 M. Nie and B. L. Lucht, Role of Lithium Salt on Solid Electrolyte Interface (SEI) Formation and Structure in Lithium Ion Batteries, *J. Electrochem. Soc.*, 2014, **161**(6), A1001–A1006, DOI: 10.1149/2.054406jes.

32 L. Yin, Z. Geng, Y. C. Chien, T. Thiringer, M. J. Lacey, A. M. Andersson and D. Brandell, Implementing intermittent current interruption into Li-ion cell modelling for improved battery diagnostics, *Electrochim. Acta*, 2022, **427**, 140888, DOI: 10.1016/j.electacta.2022.140888.

33 Z. Geng, T. Thiringer and M. J. Lacey, Intermittent Current Interruption Method for Commercial Lithium-Ion Batteries Aging Characterization, *IEEE Trans. Transp. Electrif.*, 2022, **8**(2), 2985–2995, DOI: 10.1109/TTE.2021.3125418.

34 B. Aktekin, M. J. Lacey, T. Nordh, R. Younesi, C. Tengstedt, W. Zipprich, D. Brandell and K. Edström, Understanding the Capacity Loss in $LiNi_{0.5}Mn_{1.5}O_4$–$Li_4Ti_5O_{12}$ Lithium-Ion Cells at Ambient and Elevated Temperatures, *J. Phys. Chem. C*, 2018, **122**(21), 11234–11248, DOI: 10.1021/acs.jpcc.8b02204.

35 D. Juarez-Robles, C.-F. Chen, Y. Barsukov and P. P. Mukherjee, Impedance Evolution Characteristics in Lithium-Ion Batteries, *J. Electrochem. Soc.*, 2017, **164**(4), A837–A847, DOI: 10.1149/2.1251704jes.

36 M. J. Lacey, K. Edström and D. Brandell, Visualising the problems with balancing lithium–sulfur batteries by "mapping" internal resistance, *Chem. Commun.*, 2015, **51**(92), 16502–16505, DOI: 10.1039/C5CC07167D.

37 P. Jankowski, C. Fink Elkjaer and J. Højberg, *A game-changing approach to stable cycling of LNMO-Graphite Cells*, Whitepaper, Topsoe, 2023.

